C-nanocoated ZnO by TEMPO-oxidized cellulose templating for improved photocatalytic performance

He Xiao, Yiwei Shan, Wenyao Zhang, Liulian Huang, Lihui Chen, Yonghao Ni, Bruno Boury, Hui Wu

C-nanocoated ZnO by TEMPO-oxidized Cellulose Templating for Improved Photocatalytic Performance

He Xiao [a], Yiwei Shan [a], Wenyao Zhang [c], Liulian Huang [a], Lihui Chen [a], Yonghao Ni [a,d], Bruno Boury [b*], Hui Wu [a*]

[a] College of Material Engineering, Fujian Agriculture and Forestry University, Fuzhou, 350108, China

[b] Institute Charles Gerhardt UMR CNRS 5253, CMOS team, Université de Montpellier, CC1701, place E. Bataillon, 34095, Montpellier, France

[c] Department of Chemical Engineering, University of Waterloo, Waterloo, Ontario N2L3G1, Canada

[d] Limerick Pulp and Paper Centre, Department of Chemical Engineering, University of New Brunswick, Fredericton, NBE3B 5A3, Canada

Corresponding authors: Bruno Boury (bruno.boury@univ-montp2.fr), Hui Wu (wuhuifafu@163.com)

Abstract

Ultrafine C-doped ZnO/carbon nanocomposites with different photocatalytic activities have been prepared using TEMPO-oxidized cellulose as a template but also as the source of carbon. The result is an enhancement of the photocatalytic activity ascribed

to different phenomena: a high mesoporosity beneficial to mass transport, a thin carbon layer onto ZnO increasing the charge transfer and hydrophobicity of ZnO, a narrowing of ZnO band gap and an increase of the zinc (V_{Zn}) and oxygen (V_o) vacancies effectively suppressing of the charge recombination. These are evidenced by photocatalytic test of photodegradation of methyl orange (MO) achieved to assess and compared the different photocatalysts. The highest rate constant value of photodegradation of MO is 0.0254 min^{-1}, three times higher than that of ZnO prepared without templates (0.0087 min^{-1}). The present results introduce a new vision of the use of template with multiple roles in the preparation of inorganic materials and specially photocatalysts.

Keywords: ZnO; Cellulose; Photocatalyst; Template; Carbon coating.

Introduction

Heterogeneous photocatalysis is one of the most promising processes for pollution control as well as production of chemicals and fuels(Dong et al., 2015; Lee, Lai, Ngai & Juan, 2016; Qu & Duan, 2013; Zhou, Yu & Jaroniec, 2014). Apart from TiO_2 and few others, ZnO is one of the most popular and promising semiconductors with high photocatalytic potential. It is now well documented that large exciton binding energy (60 meV), low price and low toxicity are advantages of ZnO, while major limitations are a wide band gap (3.37 eV), a high recombination rate of photoinduced electron–hole pairs and a photocorrosion with formation of zinc

hydroxide(Spathis, 1995). Among the different strategies reported to overcome these drawbacks, achieving nanosizing of ZnO particles is the simplest way to increase the proportion of active sites of the photocatalyst by increasing the specific surface area. This nanosizing also hampers the electron-hole recombination by shortening the diffusion path up to the surface of the photogenerated state. Other strategies to improve the photocatalytic activity, such as nanosizing of ZnO particles can be associated with the presence of metal, metal oxide or sulfide particles(Vaiano, Matarangolo, Murcia, Rojas, Navio & Hidalgo, 2018). Besides, combining this nanosizing with an assembly of carbon (C) to obtain a ZnO/C nanocomposites is emerging as the most attractive approach(Han, Yang, Weng & Xu, 2014). Carbon presents the desired electrical and photophysical properties acting as a temporary photoelectron reservoir to store and shuttle the photogenerated electrons from the semiconductor(Li & Cao, 2011; Samadi, Shivaee, Zanetti, Pourjavadi & Moshfegh, 2012; Yang & Xu, 2013; Zhang, Zhang, Tang & Xu, 2012). Carbon is also envisaged to improve the adsorption capability of the photocatalyst surface while improving its chemical stability as an efficient shield against corrosion.

However, these properties can deeply vary depending on the C polymorph, e.g. carbon nanotube, graphite, fullerene, graphene. Secondly, fairly different effects can be expected depending on the proportion and location of carbon, varying from a true doping of the ZnO crystal structure with an effect on the band gap(Yu, Zhang & Peng, 2016), or a photosensitization of the ZnO semiconductor(Hewlett & McLachlan, 2016), or a hydrophobization of the surface with modification of the adsorption

capacity(Hong, Lee & Ko, 2011; Yang, Weng & Xu, 2013, 2014).

Therefore, the C polymorph and its nanoassembly with ZnO are the keys for photocatalytic activity. Numerous ways to do so already exist, but there is still a need for improvements in terms of performances, sustainability, safety and cost. In this context, biopolymers are increasingly used as template and C-precursors(Boury & Plumejeau, 2015; Foresti, Vazquez & Boury, 2017). The interest in such biopolymer template ability of relies on their efficiency to bind metal cations and achieve an efficient control over the particle size of ZnO during sol-gel or solvothermal processes. Furthermore, although they are removable by calcination, these biotemplates are easily converted into highly porous C upon pyrolysis. So far, work in this area has targeted either the complete elimination of the template upon calcination, or its complete transformation into carbon upon pyrolysis. As we shall see below, we hereby propose an intermediate situation. Beside water-soluble polysaccharides like starch (Cheng, Ji, Wu & Zhang, 2016; Patrinoiu et al., 2016), alginic acid(Cheng et al., 2018), agarose (Tran, 2016)or cellulose acetate(Olaru, Calin & Olaru, 2014; Ye, Zhang, Liu & Zhou, 2011), the water insoluble cellulose is the cheapest and most available polysaccharide. In addition, it is not strategical for food supply, and useful for the preparation of ZnO(Lefatshe, Muiva & Kebaabetswe, 2017; Liu, Yao, Wang & Ma, 2017; Yuan et al., 2017; Zhao, Zuo, Guo & Pan, 2017) and many other metal oxides(Boury & Plumejeau, 2015; Foresti, Vazquez & Boury, 2017). Due to the high hydroxyl content and the presence of very few carboxylic/ate functions in its fibril surface, cellulose can efficiently coordinate metal cations(O'Connell, Birkinshaw &

O'Dwyer, 2008; Olivera, Muralidhara, Venkatesh, Guna, Gopalakrishna & Kumar, 2016; Wu, Lu, Zhang, Yuan, Xiong & Zhang, 2013; Xiong, Lu, Wang, Zhou & Zhang, 2013). Interestingly, increasing such naturally low carboxylic/ate content of natural celluloses is now easily achievable thanks to the development of the regioselective oxidation of the primary alcohol function in C6 position into a carboxylic function using the mixture of the following reagents: NaOCl/NaBr/2,2,6,6-tetramethyl piperidine-1-oxyl known as TEMPO. This chemical modification to increase the carboxylic function of cellulose has recently been reported for example to enhance the mineralization of cellulose with hydroxyapatite for bone tissues engineering (Abouzeid, Khiari, Beneventi & Dufresne, 2018; Safwat et al., 2018). We thought that this could also be an advantage in the case of the mineralization by ZnO and could afford an efficient pathway to better control the nucleation process of ZnO. We have reported the benefit of TEMPO-oxidized cellulose over pristine cellulose(Xiao, Zhang, Wei & Chen, 2018), the improvement in photocatalytic activity was attributed to the higher specific surface area obtained by controlling the growth of ZnO particles. The presence of a very low level of C was also suspected of acting as a doping agent lowering the ZnO band gap. At that point, we thought possible and attractive to modify the preparation of the material in order to achieve a deeply different nanoassembly of ZnO and C, this time targeting a true C coating of the ZnO different from a C-doping. Thanks to the use of ultrasonication during the sol-gel processing of ZnO templated by TEMPO-oxidized cellulose and to a careful control over the temperature during the calcination that preserve a thin layer of C, we are now able to

report here the formation of a C-coated ZnO with very high photocatalytic activity. The general strategy of preparation of the samples is summarized in Figure 1, in addition to the complete characterization of materials, we present a comprehensive study of the photocatalytic process of degradation with methyl orange, an identification of the role of the C layer and a comparison with other C-doped ZnO.

Materials and methods

Materials

Zinc nitrate hexahydrate ($Zn(NO_3)_2 \cdot 6H_2O$), urea (CH_4N_2O), sodium hypochlorite (NaClO), sodium bromide (NaBr) and sodium hydroxide (NaOH), hydrochloric acid (HCl) and ethanol (CH_3CH_2OH) were of analytical grade and utilized without purification. The above chemicals were acquired from Shanghai Macklin Biochemical Co.,Ltd. 2,2,6,6-tetramethylpiperidine-1-oxyl (TEMPO) agent (≥98%) and methyl orange (MO) (≥96%) were obtained from Aladdin Industrial Corporation. Bamboo dissolving pulp (α-cellulose ≥94%) was obtained from Fujian Qingshan Paper Industry Co., Ltd and was used without pretreatment before experiment.

Preparation of TEMPO-oxidized cellulose (TOC)

The TEMPO-oxidized cellulose was prepared from bamboo pulps according to the previously reported method(Sehaqui, Zhou, Ikkala & Berglund, 2011): Bamboo pulp (2.00 g) was suspended in deionized water (200 mL) at room temperature (25 °C) using mechanical stirring (400 r/min) for 1 h. Then TEMPO agent (0.04 mmol g^{-1} of

dried cellulose) and sodium bromide (NaBr, 0.4 mmol g^{-1} of dried cellulose) were successively added into the above suspension. Then, sodium hypochlorite (NaClO, 12 mmol g^{-1} of dried cellulose) was added dropwise to the mixture. During the TEMPO-oxidized process, the pH of the mixture was maintained at 10 by adding NaOH (0.1 M) with continuous stirring for 6 h. The obtained suspension was homogenized by sonication（FS-1200N）at 25°C for 5 min with ultrasonic power (1000W), and then centrifuged at 9000 r min^{-1} for 15 min. The solid residue was recovered, and impurities were thoroughly washed through abundant dilute hydrochloric acid (0.1 M) and deionized water repeatedly. The as-prepared sample, labeled as TOC, was stored at 4°C as an aqueous dispersion for further experiments. Non-oxidized cellulose of bamboo dissolving pulp was denoted as NOC. Carboxyl contents in the different cellulose were determined by the electric conductivity titration method(Jiang & Hsieh, 2013).

Preparation of TOC-templated ZnO (TOC-ZnO) and template-free ZnO (FT-ZnO) and cellulose-templated ZnO (NOC-ZnO)

TEMPO-oxidized cellulose TOC (1.89 g, 11.67 mmol, 1wt % water suspension) was dispersed in 100 mL deionized water for 30 min at room temperature (25°C). After that, $Zn(NO_3)_2{\cdot}6H_2O$ (2.97 g, 10 mmol) was previously dissolved in 40 mL deionized water, then added into the TOC suspension with continuous stirring (400 r/min) for 1 h at 25 °C. Subsequently, urea (0.36 g, 6 mmol, 0.6 mol L^{-1} water solution) was dropwise added into the mixtures with ultrasonic process (FS-1200N, 1000 W, 25°C)

for 5 min, then heated in an oil bath at 90°C for 3 h leading to the formation of a white suspension. The latter was then repeatedly washed with 500 mL deionized water five times in a row, centrifuged at 8000 r min^{-1} and vacuum dried at 60 °C for 24 h labeled as TOC-ZnO. For comparison, pure ZnO and ZnO/unmodified cellulose composites were prepared according to the same procedure as described above FT-ZnO and NOC-ZnO, respectively.

Preparation of calcined sample TOC-ZnO^{x}, (x = 300, 400, 500, 600) and TF-ZnO^{400} and NOC-ZnO^{400}

TOC-ZnO were calcined at different temperatures (300°C, 400°C, 500°C, 600°C) in muffle furnace in steady conditions without any air stream or addition for 2 h and then cooled down quickly in laboratory atmosphere leading to samples respectively labeled as TOC-ZnO^{300}, TOC-ZnO^{400}, TOC-ZnO^{500} and TOC-ZnO^{600}. TF-ZnO and NOC-ZnO were similarly calcined at 400°C in air atmosphere for 2 h denoted as TF-ZnO^{400} and NOC-ZnO^{400}, respectively.

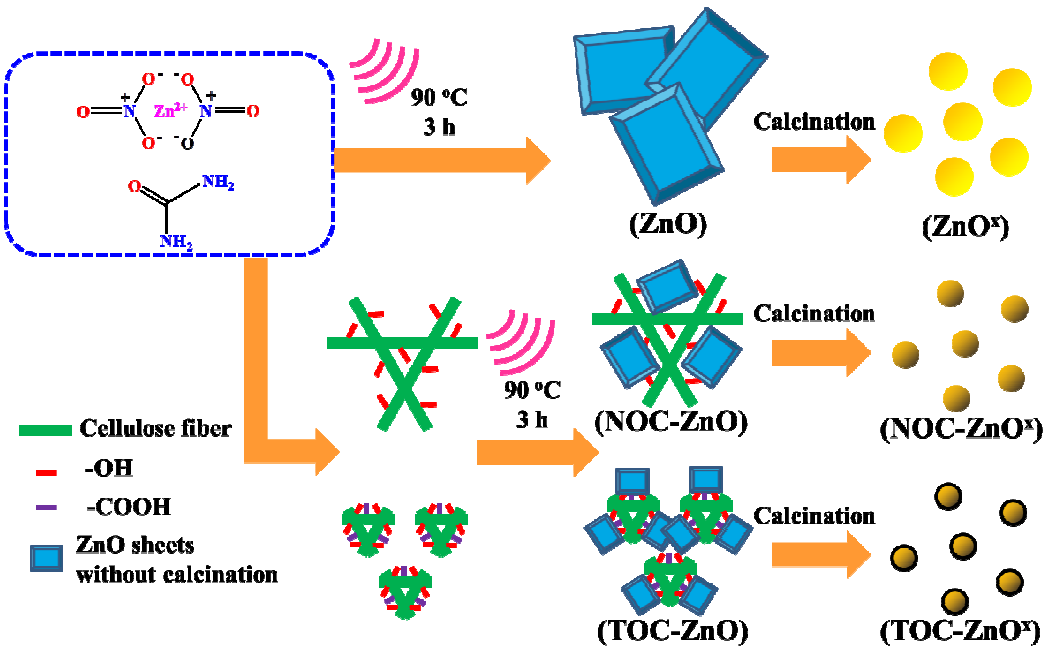

Fig.1. Schematic illustration of the concept and general procedure for the preparation of C-covered ZnO nanocrystals templated by TEMPO-oxidized cellulose.

Photocatalyst characterization

TEMPO-oxidized cellulose was analyzed by fiber analyzer (Techpap， MorFi Compact，France) to characterize the length and width. Fourier transform infrared (FT-IR) spectra were measured by an FT-IR spectrometer equipped with an ATR accessory (Pekin-Elmer, 1600, USA) ranging the wavelength from 4000 cm^{-1} to 400 cm^{-1}. The zeta potential of 0.1 wt% aqueous bamboo dissolving pulp (NOC) and TEMPO-oxidized cellulose (TOC) suspensions were recorded with a Zetasizer Nano ZS90 analyzer (Malvern, Britain). The thermogravimetric analysis (TGA) curves were performed using STA-449 thermogravimetric analyzer (Netzsch, Germany) with a temperature range of 25-700°C at a heating rate of 10 °C·min^{-1} in air flow (50 mL·min^{-1}). Raman scattering spectra were recorded on Invia Reflex Raman

185 Microscopy (Renishaw, UK) equipped with a 532 nm laser source. X-ray diffraction
186 (XRD) analyses were recorded out by X-ray diffractometer (Rigaku, Ultima Ⅳ, Japan)
187 using Cu Kα radiation, tube voltage 40 kV and tube current 45 mA. Contact angle
188 testing was measured by a dynamic drop tension meter (DSA 30, KRUSS, Germany).
189 ZnO-based photocatalysts were coated and adhered to slide glasses with tapes. Then 5
190 μL of water drop was placed on the surface of the photocatalysts to investigate the
191 contact angle. A field emission scanning electron microscope (Hitachi, SU8010, Japan)
192 was used to observe the morphologies of carbon-doping ZnO samples. The detailed
193 microstructures of ZnO nanocrystals were investigated by using a transmission
194 electron microscopy (JEOL, JEM-2100, Japan) with a field emission gun operating at
195 200 kV. The chemical compositions of ZnO nanocrystals were determined by energy
196 dispersive spectroscopy (HORIBA, XMX 1011, Japan). Total organic carbon content
197 of calcined samples was measured by elemental analyzer (Vario EL cube, Elementar,
198 Germany). X-ray photoelectron spectra (XPS) were measured using an ESCALAB
199 250 instrument (Thermo Scientific, USA) with Al Kα radiation monochromatic source.
200 The valence band (VB) values were detected by XPS scanning from 0~10 eV with
201 0.05 eV recording once. The specific surface area and pore characteristics of ZnO
202 nanocrystals were determined by N_2 adsorption-desorption measurements
203 (Micromeritics, ASAP 2020, USA). Diffuse reflectance UV-Vis (DR UV-Vis) spectra
204 were recorded on Cary 500, Varian Corporation. Electron paramagnetic resonance
205 (EPR) measurements were carried out by an EMXnano spectrometer (Bruker,
206 Germany) operating at 77 K with a frequency of 9.4 GHz. The photoluminescence

spectroscopy (PL) spectra of the samples were recorded using LS55 spectrophotometer (Perkin-Elmer, USA) with 325 nm excitation wavelength. The electrochemical impedance spectroscopy measurement was performed at VersaSTAT MC electrochemical workstation (Princeton, USA). The measurement was carried out in a three-electrode cell with a glassy (FTO) carbon electrode as the working electrode, Ag/AgCl as the reference electrode and Pt plate as the counter electrode.

Evaluation of photocatalytic activity

The ultraviolet light source is a 6 W lamp with the wavelength range of 200-400 nm (Beijing Zhong Jiao Jin Yuan Technology Co., Ltd.). And the distance between the light source and the reaction tube was fixed as 10 cm(Zhao, Zuo, Guo & Pan, 2017). ZnO-based photocatalyst (25 mg, 0.309 mmol) were added into methyl orange solution (5 mg L^{-1}, 100 mL) with continuously stirring (300 r/min) at 25°C for 30 min in dark conditions in order to reach the adsorption-desorption equilibrium. Then, light irradiation was turned on and aliquots (4 mL) were withdrawn and filtered through PES membrane (Jin Teng Experimental Equipment Co., Ltd., 13×0.22 μm, 0.22 μm pore size, Tianjin, China) at 15 min, 30 min, 60 min, 90 min and 120 min, respectively. The MO concentration of the filtrate was measured by UV-Vis spectrophotometer (Shimadzu, UVmini-1240, Japan) at 463 nm. To investigate the photocatalytic stability of TOC-ZnO^{400} was used in five consecutive cycles with centrifugal separation (washing by deionized water three times and vacuum drying at 40°C for 12 hours) after each one. The XRD characterization of the photocatalyst after five cycles

was also detected by X-ray diffractometer.

Results and discussion

Synthesis and Characteristics of TOC-ZnO, FT-ZnO and NOC-ZnO. Submicron fibrils of bamboo pulp cellulose were used for controlling morphology, porosity and growth of ZnO nanoparticles. Prior to reaction with zinc nitrate in urea solution, selective oxidation of the primary alcohol in the C6 position was performed with TEMPO in basic medium to increase the carboxylic/ate content(Isogai, Saito & Fukuzumi, 2011; Pierre et al., 2017). Using the electric conductivity titration method, the proportion of this group in TOC was estimated to 1.51 mmol g^{-1}, much higher than the initial proportion of 0.1 mmol g^{-1} for NOC. This significant increase in the number of carboxylate groups is a decisive element allowing a greater control of the intermediate ZnO growth in the form of a nanoparticle more homogeneously distributed along the fibers (see calculation of this distribution in Table S1).

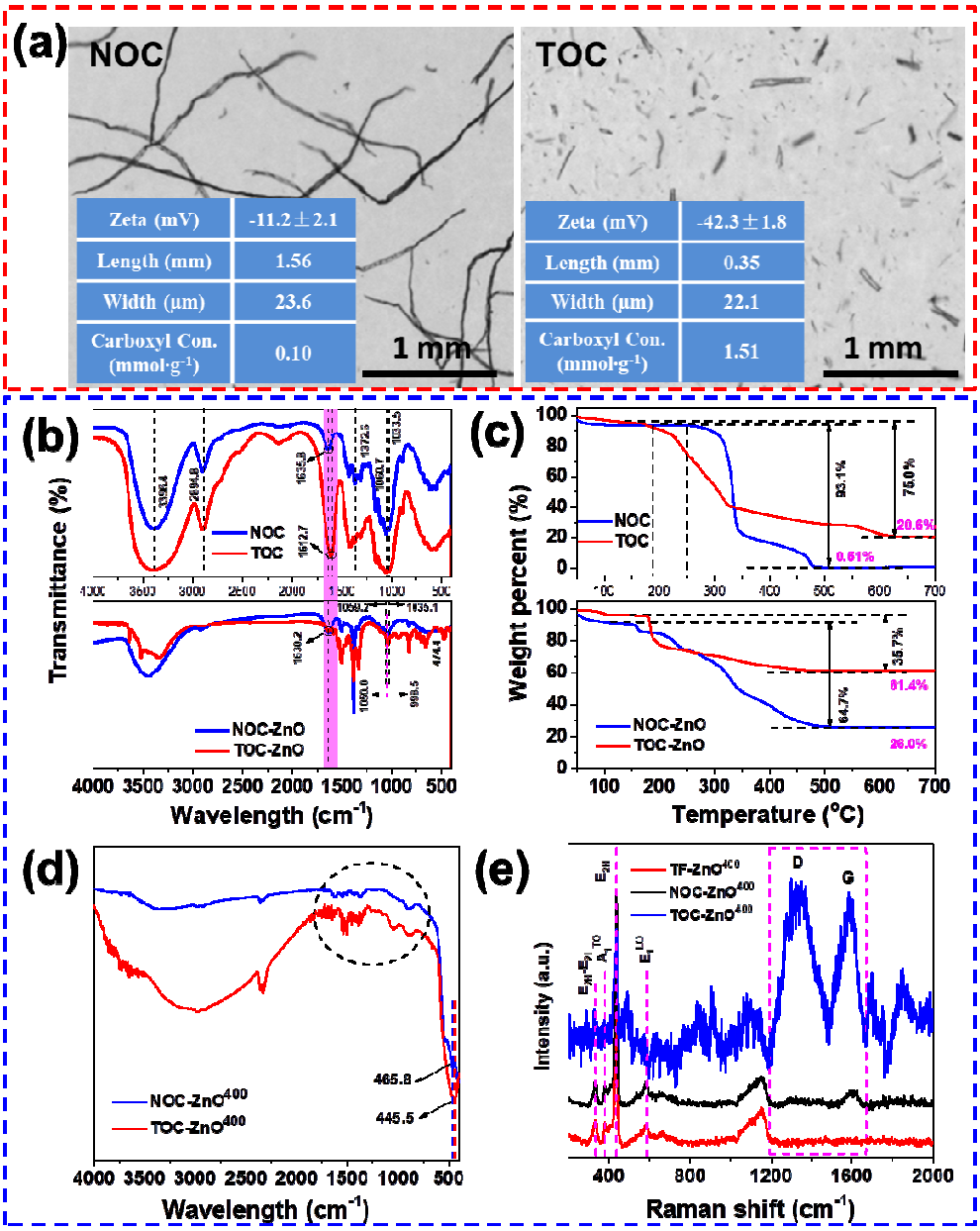

243

244 **Fig.2** Images and main characteristics of pure cellulosic fibers and TOC (a), FT-IR spectra of

245 cellulosic fibers and ZnO samples (b), Thermograms of cellulosic fibers NOC and TOC and of

246 ZnO samples (c), FT-IR spectra of ZnO^{400} samples (d), Raman spectra of three different ZnO^{400}

247 samples (e).

248

249 The size and morphologies of cellulose fibers before and after TEMPO-oxidized

250 treatment are shown in Figure 2-a,b. As observed by other(Cao, Ding, Yu & Al-Deyab,

2012), it is clear that the TEMPO treatment results in a shortening of the length of pristine cellulose (NOC), the latter being frequently ten times longer than the whiskers-like TEMPO-oxidized cellulose (TOC). However, the average width is apparently not modified by the TEMPO treatment. Thus, it indicates that the side reactions of TEMPO oxidation that lead to chain scission occurred mainly in some specific part of the fibers resulting in their scission and subsequent length reduction. The amorphous domains of the cellulose fiber are candidates for this as observed in other chemical treatment of cellulose, e.g. acidic hydrolysis. A consequence of the chemical modification is an important decrease of the Zeta potential from -11.2 mV for NOC to -42.3 mV for TOC resulting from the increase of anionic carboxylate groups on the surface of the TEMPO-oxidized cellulose.

The ZnO-containing materials were prepared by solvothermal process in mild condition (3 h, 90°C) either without cellulose, or with cellulose or with TEMPO-oxidized cellulose (Figure 1). The FTIR spectra of NOC and TOC are compared in Figure 2-b. Several characteristic peaks are similar, especially those at 3396.4 cm^{-1}, 2894.8 cm^{-1} and 1372.6 cm^{-1} respectively due to O-H and C-H stretching vibrations and C-H asymmetric deformations. Besides, the C-O stretching vibrations are slightly shifted from 1060.7 cm^{-1} for C to 1033.5 cm^{-1} for TOC. However, the major difference between both samples is the position and intensity of the C=O stretching frequency of carboxylate groups of NOC (1635.8 cm^{-1}) and TOC (1612.7 cm^{-1}), both phenomena being related to the TEMPO oxidation. For NOC-ZnO the characteristic peak at 1059.2 cm^{-1} and 1035.1 cm^{-1} are respectively assigned to

glucose ring skeletal vibration and C-O stretching vibration peak. These bands are shifted for TOC-ZnO respectively to 1049.1 cm^{-1} and 992.3 cm^{-1}, this being ascribable to H-bonding between cellulose and oxo- or hydroxo-Zn species in nanoparticles(Ali et al., 2016). Due to the limit of the spectrometer, the maximum of band absorption for the stretching mode of ZnO at 431 cm^{-1} is not observed.

To evaluate the relative proportions of cellulose and ZnO in the TOC composite, thermogravimetry analysis was performed on NOC, TOC, NOC-ZnO and TOC-ZnO, (Figure 2-c). Weight loss starts earlier for TOC (180-190°C) than for NOC (250°C), this results from possible esterification of the abundant carboxylic and hydroxyl groups in TOC compared to NOC. It can also be ascribed to dehydration between residual Zn(OH) functions. For NOC alone, a 99.5% weight loss by 700°C is measured, much higher than the weight loss for TOC, of up to 79.4%. This is ascribed to the presence of sodium carboxylate and its decomposition upon pyrolysis result in sodium oxide. When nano-assembled with ZnO, the situation is very different, and TGA curves reveal that a much higher proportion of ZnO is assembled with TOC (40.8% yield at 700°C for TOC-ZnO) compared with NOC (25.5% yield at 700°C for C-ZnO). Additionally, these analyses indicate that the decomposition of cellulose is almost complete by 500°C. Indeed, after thermal treatment at 400ºC, FTIR analysis in figure 2-d shows tiny peaks ranged from 1800 to 1000 cm^{-1} that cannot be attributed to ZnO and are ascribed to carbonaceous residue issued from NOC or TOC. The Zn-O stretching vibration peaks at 465.8 cm^{-1} for NOC-ZnO^{400} and 445.5 cm^{-1} for TOC-ZnO^{400} are blue-shifted compared to the TF-ZnO^{400} (474.4 cm^{-1}), which is

ascribable to the smaller crystal size after the template preparation process(Yu, Chen, Wang & Yao, 2015).

To further investigate the characteristics of the samples, the Raman spectra of TF-ZnO^{400} (Figure 2-e) show that four main peaks at 331.4 cm^{-1}, 380.8 cm^{-1}, 437.4 cm^{-1} and 584.4 cm^{-1} were assigned to E_{2H}-E_{2L}, A_1^{TO}, E_{2H} and E_1^{LO}, respectively. In the spectra of NOC-ZnO^{400} and TOC-ZnO^{400}, the peaks of E_{2H}-E_{2L}, A_1^{TO} and E_1^{LO} are all blue-shifted, respectively 329.5 cm^{-1} and 326.2 cm^{-1} for E_{2H}-E_{2L}, 378.9 cm^{-1} and 374.8 cm^{-1} for A_1^{TO} and finally 582.6 cm^{-1} and 574.4 cm^{-1} for E_1^{LO}. A possible explanation is the presence of a doping phenomenon as frequently reported to explain blue shift in metal oxides like ZnO(Beltran, Barrero & Punnoose, 2019). Carbon arising from the residue of cellulose is one candidate as evidenced by EDX analyses given below. Besides, an important feature of the Raman spectrum of TOC-ZnO^{400} is the presence of two dominant peaks at approximately 1340 cm^{-1} and 1590 cm^{-1}, usually attributed to D and G signals of graphitic carbon structure. The broadness and the low intensity of the signals indicate two important points: first the thinness of the carbon domain, and secondly the highly disordered structure of the graphitic carbon. An expected situation if considering the low temperature of calcination. However, this is clearly different from NOC-ZnO^{400} and TF-ZnO^{400} for which no signal in these regions are observed.

The EDX analysis confirms the effect of the cellulosic oxidized template on the composition of the material, namely the presence of residual carbon: 1.09% in TOC-ZnO^{400}, 0.47 % in NOC-ZnO^{400} and only 0.23% in TF-ZnO^{400}, given in Fig.S1.

In the latter, the total organic carbon from quantitative element analysis gives slightly different values: 0.45% in TOC-ZnO^{400}, higher than 0.14% for NOC-ZnO^{400} and 0.05% for TF-ZnO^{400}. Surface contamination by CO_2 and carbonate-related species can explain the higher values obtained by EDX. However, the high C-contents are clearly related to the use and decomposition of cellulosic template, samples were gold-coated for analysis. The presence of such residual carbon is further demonstrated below by the TEM images. This can result from the fact that tiny parts of the cellulosic template are not fully accessible to oxygen and are carbonized but not further oxidized into CO_2 and water. This phenomenon is favored by the relatively low temperature of calcination used here (400°C) and the absence of any air stream in the furnace, however, the reason why the TEMPO-oxidized cellulose leads to higher C-content is not understood at present.

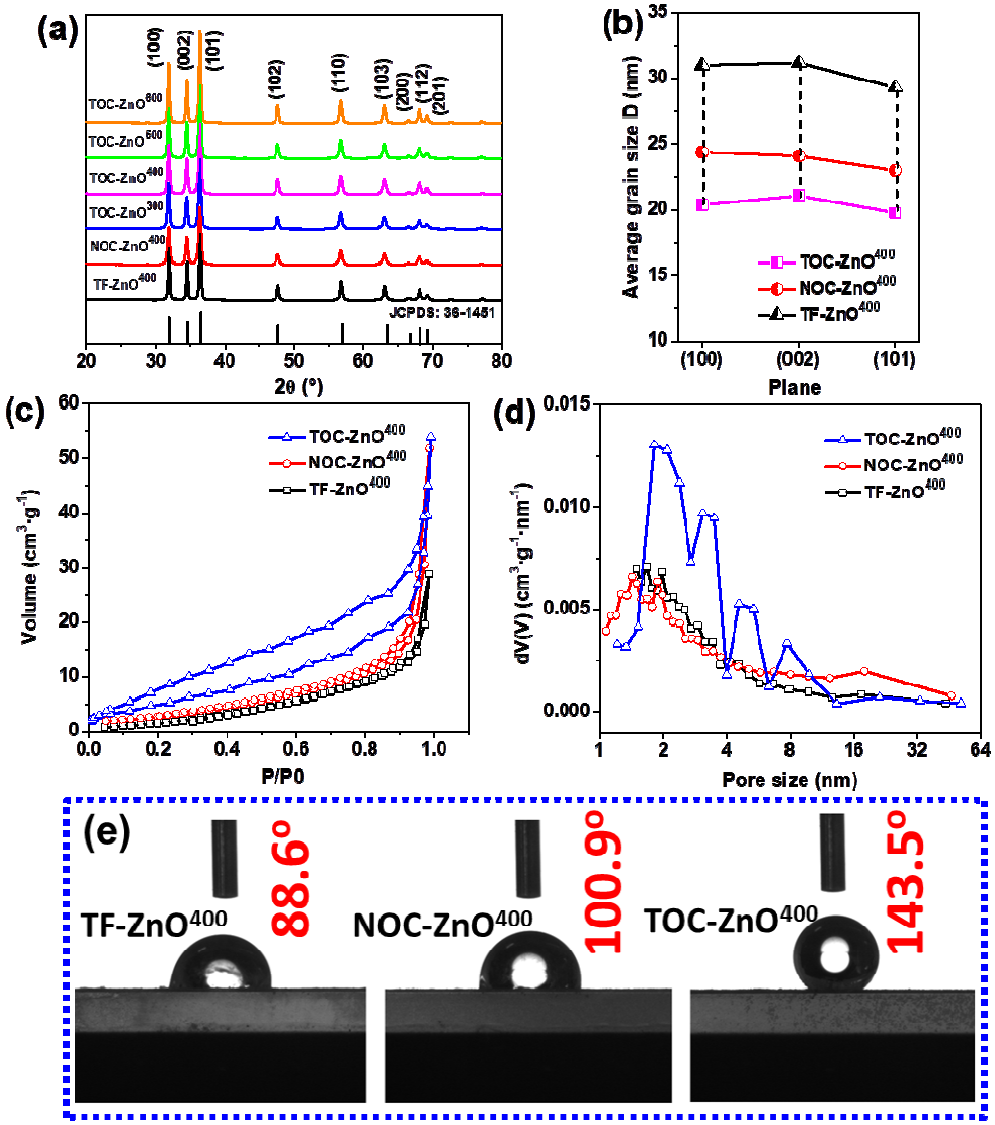

329

330 **Fig.3** Powder XRD patterns of samples after calcination (a) and average grain size (D) of (100),

331 (002) and (101) for TF-ZnO^{400}, NOC-ZnO^{400} and TOC-ZnO^{400} (b), N_2 adsorption-desorption

332 isotherms (c), pore size distribution derived from desorption isotherm of TF-ZnO^{400}, NOC-ZnO^{400}

333 and TOC-ZnO^{400} (d) and micrographs of contact angles measurements of TF-ZnO^{400},

334 NOC-ZnO^{400} and TOC-ZnO^{400} (e).

335

336 For all the samples, the X-ray diffraction pattern is in good accordance with the

337 characteristic of the hexagonal wurtzite structure ZnO (JCPDS 36-1451) with

characteristic peaks at 31.90°, 34.56°, 36.40°, 47.68°, 56.74°, 63.00°, 66.50°,68.08°, 69.22° indexed to (100), (002), (101), (102), (110), (103), (200), (112), (201) planes respectively (Figure 3a, Table S2). However, the TOC-ZnO without calcination contained ZnO with lower crystallinity as evidenced in Fig.S2. Moreover, other signals of the patterns could be attributed to zinc(II) hydroxocarbonate [$Zn_4(OH)_6CO_3$] (PDF: 19-1458). The presence of the latter is important for further understanding of the evolution, characteristics and performances of the material after calcination.

The effect of cellulose template on the properties of ZnO is also revealed by the values of specific surface area, pore volume and pores distribution obtained from nitrogen porosimetry measurements and shown in Figure 3c, d and Table S3. The adsorption-desorption isotherms of TF-ZnO^{400}, NOC-ZnO^{400} and specially TOC-ZnO^{400} corresponded to the type IV curve with a H3 hysteresis loop, which confirms the mesoporous nature of all the samples probably arising from intergranular voids. From Figure 3d, as supported by the broad hysteresis loop, TOC-ZnO^{400} is clearly less microporous than TF-ZnO^{400} and NOC-ZnO^{400} showing an important proportion of pore with $\varnothing$<2 nm, and a higher proportion of mesopores 2 <$\varnothing$<≈20 nm. From Table S3, the specific surface area and pore volume of as-prepared ZnO samples was as follows: TF-ZnO^{400}<NOC-ZnO^{400}< TOC-ZnO^{400}. There are four possible driving forces for the formation of mesopores. Part of it can initially originate from inter-particles voids left between the vicinal nanoparticles attached to cellulose, this can be seen as an effect of the cellulose hard templating. Secondly, during the calcination, these nanoparticles are prevented from collapse and sintering by the

presence of the carbon residues and layer (Fig.S1) that also can result in mesoporosity. Thirdly, either during the hydrothermal process, or during the calcination if some urea residues are included in the pre-calcined ZnO nanoparticles, their decomposition generates CO_2 can also result in pore formation. This can also occur during the thermal decomposition of the Zinc(II) hydroxocarbonate (identified in X-ray diffraction pattern, Fig. S2) that is evidenced before calcination, and which decomposition can occur by multistep mechanisms (see in Fig.S3). Another effect of the use of TOC instead of NOC is a deep change of the hydrophobic/hydrophilic balance of the material surface. As shown in Figure 3e, the contact angles of TOC-ZnO^{400} (143.5°) were far larger than TF-ZnO^{400} (88.6°) and NOC-ZnO^{400} (100.9°) demonstrating the higher hydrophobicity of the surface of TOC-ZnO^{400} and an additional evidence of its specificity. However, the powder formed stable mixture in solution of the photocatalytic test as the result of the stirring and possibly of a light photocatalytic oxidation of the C-layer taking place during the beginning of the test and leading to a reduced hydrophobicity.

As a primary conclusion on the synthesis of the photocatalyst, it is possible to underline the major effect and advantages of TOC as template in the synthesis of ZnO. First, TOC combined with ultrasonic activation severely limits the growth of ZnO nanocrystals. The abundant carboxyl/ate groups of the TOC probably act as efficient Zn(II) binding sites that increase the number of seeding sites and decrease the ZnO particles size and their aggregation. The massive elimination of TOC upon calcination leads to higher specific surface area and porous volume, both beneficial to drive high

mass transfer during the photocatalytic process. However, the low temperature of calcination (400°C) allows preserving a thin carbon layer coating the ZnO nanocrystals.

The average grain size determined using typical crystal planes (100), (002) and (101) for TF-ZnO^{400} are found to be similar ≈30 nm (Figure 3b). The average grain size of the characteristic planes of NOC-ZnO^{400} and TOC-ZnO^{400} is lower by 22% and 33% respectively. This indicates that a cellulose template is very effective in reducing crystal growth and agglomeration of primary grains, especially if carboxylate groups have been increased like in TOC as expected; the peak positions of (100), (002) and (101) have negatively shifted with the increase of the temperature of calcination but the average grain size increase by 10-50% in Table S2. Such 2θ shift is attributed at present to the presence of carbon, either as a C-layer or a C-doping, that can generate strain upon calcination. It has been reported that for a nanocrystalline material subjected to a strain, diffraction peaks can be either broadened (due to nonuniform strain, “strain broadening”) and/or shift toward high-2θ value (for uniform compressive strain) or low-2θ value (for uniform tensile strain)(Cullity, 1978).

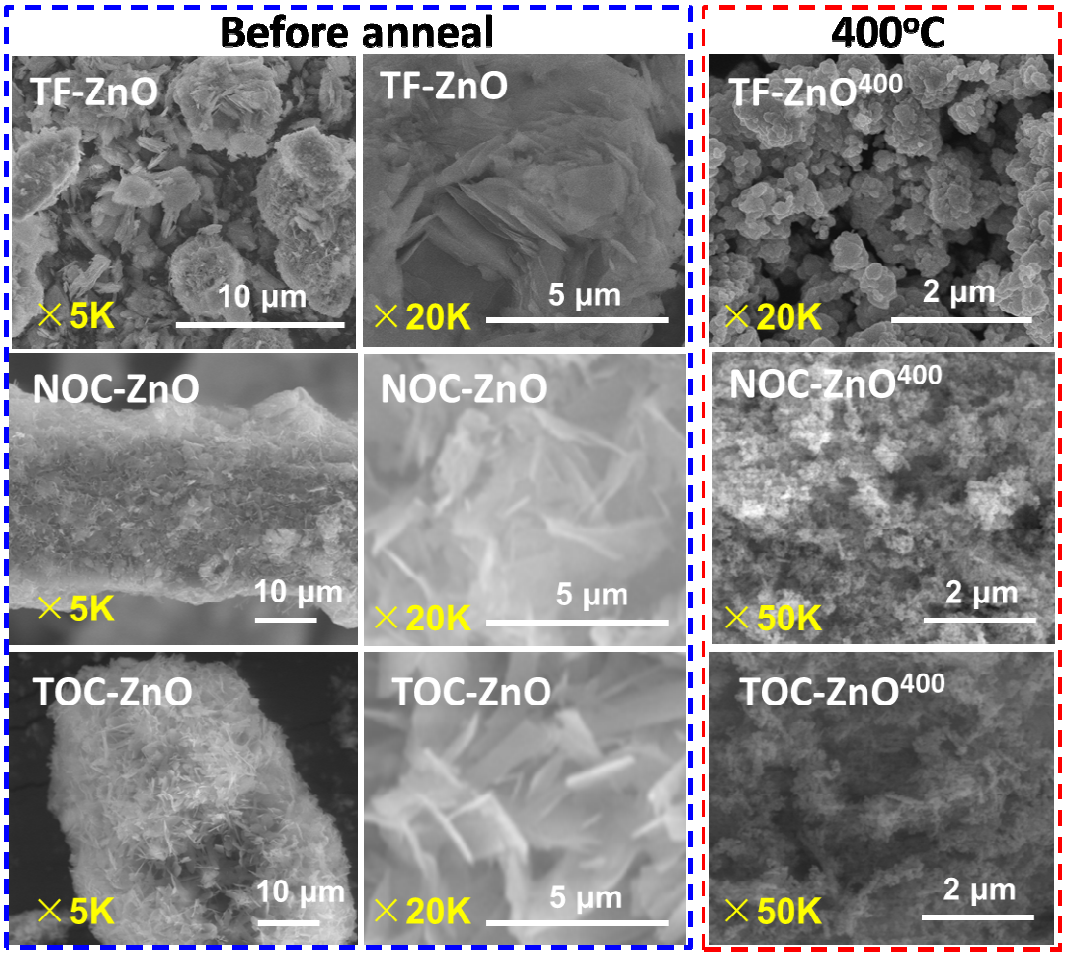

399

400 **Fig.4** SEM images of TF-ZnO, NOC-ZnO and TOC-ZnO before and after thermal treatment at

401 400°C.

402

403 The effect of the cellulose on the morphology of ZnO is evidenced by SEM

404 analysis of samples before calcination (Figure 4) and has consequences on the sample

405 afterward. As shown in Figure 4, large and disordered flake-like aggregates (2~4 μm)

406 of ZnO are obtained in the absence of any template. The presence of NOC or TOC

407 results in a uniform deposit of smaller flakes on the surface of the cellulose template;

408 interestingly they are smaller when using TOC (~1 μm) rather than NOC (1~2 μm).

409 After calcination and removal of the cellulosic template, the original aggregates are

transformed. The calcination introduces major modifications with the increase of the temperature (300~600°C) as shown in Fig.S4; especially, the ZnO morphologies change from flakes to nanorods and to coarse rounded nano- and macro-particles, their size gradually increasing with temperature.(Li, Lan, JianPing, XiaoSong, HaiYan & JinYan; Zhao, Zuo, Guo & Pan, 2017). This modification of morphology corresponds, at least partially, with the thermal decomposition of loose flake-like basic zinc carbonate [$Zn_4(OH)_6CO_3$] resulting in ultrafine ZnO with classical nanorod morphology.

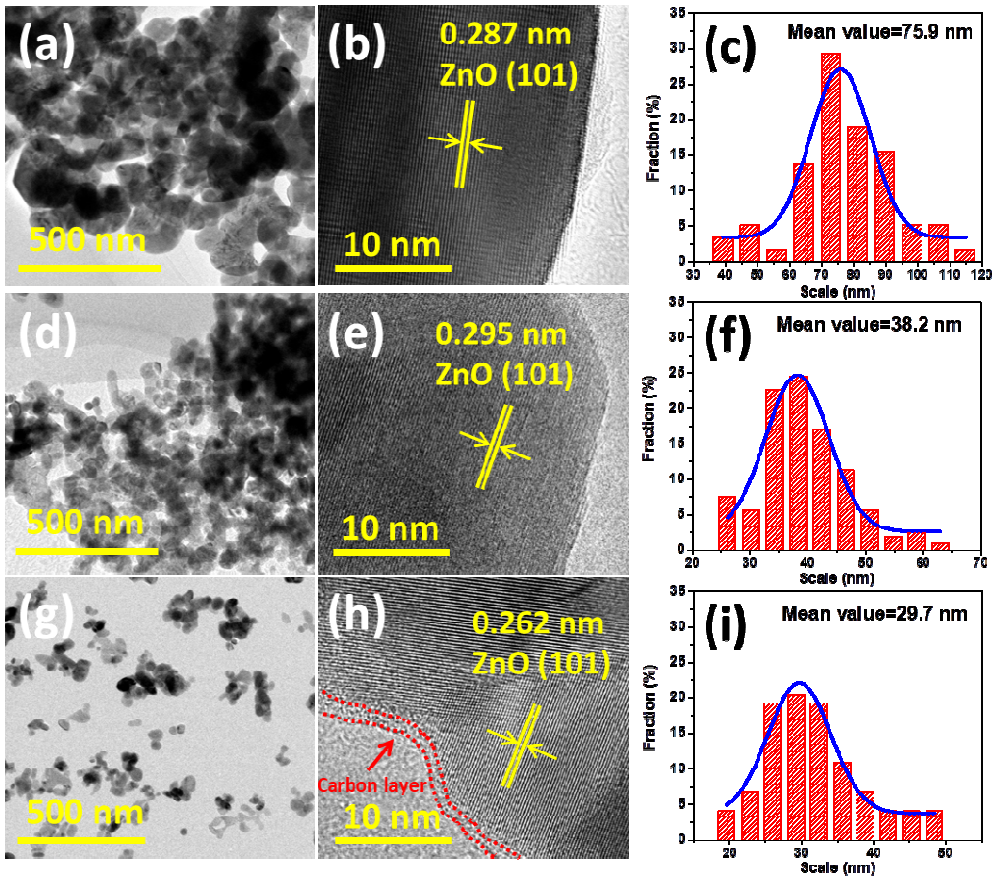

Fig.5 TEM images and particle size distribution of TF-ZnO^{400} (a, b and c), NOC-ZnO^{400} (d, e and f), and TOC-ZnO^{400} (g, h and i).

At lower scale, TEM images (Figure 5) further demonstrate the effect of the cellulosic template. When absent, the corresponding sample FT-ZnO^{400} presents ZnO nanoparticles size ≈40-200 nm (average size=75.9 nm), much larger than the nanoparticle size of NOC-ZnO^{400} and TOC-ZnO^{400} ≈20-100 nm. Both values are higher than the crystallite size determined by X-ray analysis suggesting that the particles may not be completely crystallized or made of several crystallites. Beside the size decreasing with the effect of cellulose template, lattices fringes have also narrowed. In Figure 5-b and 5-e, the lattices fringes (101) measurement is 0.287 nm for NOC-ZnO^{400} a lower value compared to 0.295 nm determined for TF-ZnO^{400}. A possible reason of that is a carbon doping in the ZnO and the XRD position (101) has slightly blue shift. Meanwhile, the lattices fringes (101) of TOC-ZnO^{400} have reduced to 0.262 nm, that is mainly caused by the presence of abundant oxygen defects in the ZnO (Liu et al., 2014). Very importantly, at the highest magnification, a thin layer of disorder carbon with thickness ≈ 1-3 nm, can be identified especially in boundary area and surrounding the dense ZnO particles.

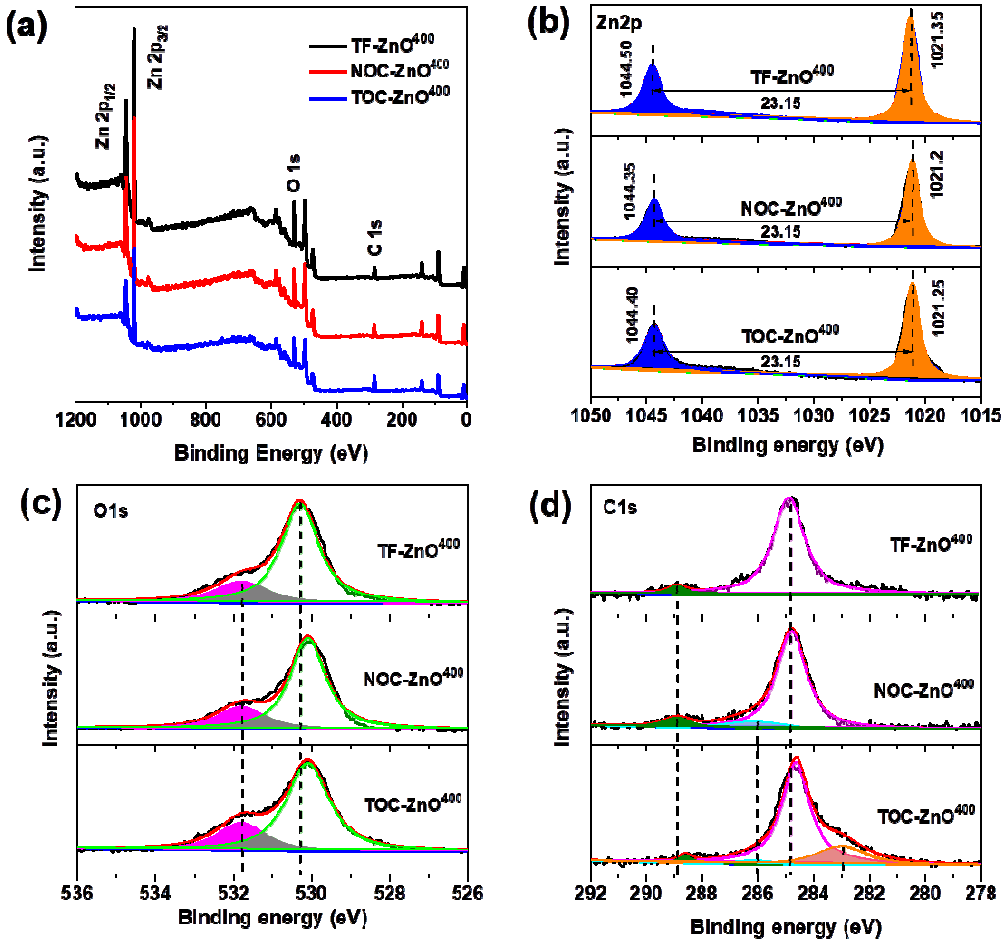

438

439 **Fig.6** XPS data of TF-ZnO^{400}, NOC-ZnO^{400} and TOC-ZnO^{400} samples: survey scan (a) and core

440 spectra with deconvolution for Zn-2p, (b) O-1s, (c) C-1s, (d).

441

442 To confirm the elemental composition and chemical states of the samples, XPS

443 spectra are reported in Figure 6 for samples calcined at 400°C. Two peaks at 1021.35

444 eV and 1044.50 eV are attributed to Zn $2p_{3/2}$ and Zn $2p_{1/2}$ levels of Zn(II). For the

445 NOC-ZnO^{400} and TOC-ZnO^{400}, these binding energies are slightly negatively shifted,

446 which is due to the different chemical interactions(Ansari, Ansari, Foaud & Cho,

447 2017). Besides, the binding energies gap between Zn $2p_{3/2}$ and Zn $2p_{1/2}$ of all the ZnO

448 samples are similar at 23.15 eV, a clear indication that the Zn atoms are in a

449 completely oxidized state. For O1s (Figure 6-c), deconvolution leads to two signals
450 one binding energy at 531.8 eV corresponding to -OH group and one at ~530.3 eV
451 corresponding to lattice oxygen Zn-O(Kotsis & Staemmler, 2006). The latter, in the
452 case of NOC-ZnO^{400} and TOC-ZnO^{400} is 0.2 eV lower because of chemical
453 interactions present in the samples(Ansari, Ansari, Foaud & Cho, 2017). As
454 summarized in Table S4, the content of the hydroxyl group for NOC-ZnO^{400} and
455 TOC-ZnO^{400} is slightly higher than in TF-ZnO^{400}. Meanwhile, the content of lattice
456 oxygen decreased relatively. The C1s high resolution spectra of TF-ZnO^{400} can be
457 divided into two peaks at 288.90 eV and 284.90 eV, while those of NOC-ZnO^{400} and
458 TOC-ZnO^{400} can be deconvoluted into three peaks (288.90 eV, 286.10 eV and 284.80
459 eV) and four peaks (288.60 eV, 286.10 eV, 284.65 eV and 283.00 eV) shown in Table
460 S5. For all the samples, the peaks located at ~288.90 eV and ~284.90 eV could be
461 assigned to the adsorbed CO_2 and graphitic sites (forming C-C group),
462 respectively(Pan et al., 2016). The satellite peak centered at 283.0 eV might be
463 attributed to the O-Zn-C bonds because of the presence of oxygen
464 vacancies(Alshammari et al., 2015; Mishra et al., 2013) and the peaks at 286.10 eV
465 for NOC-ZnO^{400} and TOC-ZnO^{400} might be attributed to Zn-O-C bonds(Zhang et al.,
466 2015a).
467
468 *Evaluation of the photocatalytic activity.* The photocatalytic activities of all the
469 samples were evaluated by photodegradation of methyl orange (MO) under UV light
470 irradiation. From figure 7-a and Table S6, the adsorption of MO on all the samples

were less than 3% after a 30 min dark adsorption. From a general point of view, the photocatalytic activity follows the order TOC-ZnO^{400} > NOC-ZnO^{400} > TOC-ZnO^{300} > TF-ZnO^{400} > TOC-ZnO^{500} > TOC-ZnO^{600}. After 120 min of photodegradation, 95.4% of MO was removed by TOC-ZnO^{400}, while the NOC-ZnO^{400} and TF-ZnO^{400} only degraded 74.8% and 65.9% of MO, respectively. Besides, photodegradation of MO by TF-ZnO, NOC-ZnO and TOC-ZnO before calcination was only respectively 5.4%, 6.8% and 7.5% after 120 min UV light irradiation in Fig.S5, which shows that proper calcination treatment improves the photocatalytic activities by the conversion of the Zinc(II) hydroxocarbonate into ZnO, and by enhancing the crystallinity of the material. Figure 7-b displays that photocatalytic rate of TOC-ZnO^{400} was up to 2.54×10^{-2} min^{-1}, which is 2.2 times and 2.9 times that of NOC-ZnO^{400} and TF-ZnO^{400}. This can be partially correlated with the higher specific surface area of TOC-ZnO^{400} (see Table S3) the rate constants (k'_{app}) for TOC-ZnO^{400} being both 1.3 times that of TF-ZnO^{400} and NOC-ZnO^{400} (see Table S6). Importantly, this set of data points out that there is an optimum for the temperature of calcination, indeed rate constants for ZnO annealed at lower (300°) or higher (500 and 600°C) temperature are $<1\times10^{-2}$ min^{-1}, lower than the one for a calcination performed at 400°C. Compared with other reported literatures in Table 1, TOC-ZnO^{400} appears as a very attractive materials avoiding the use of leachable heavy metal like Cu and very efficient a very low concentration (0.25 mg L^{-1}).

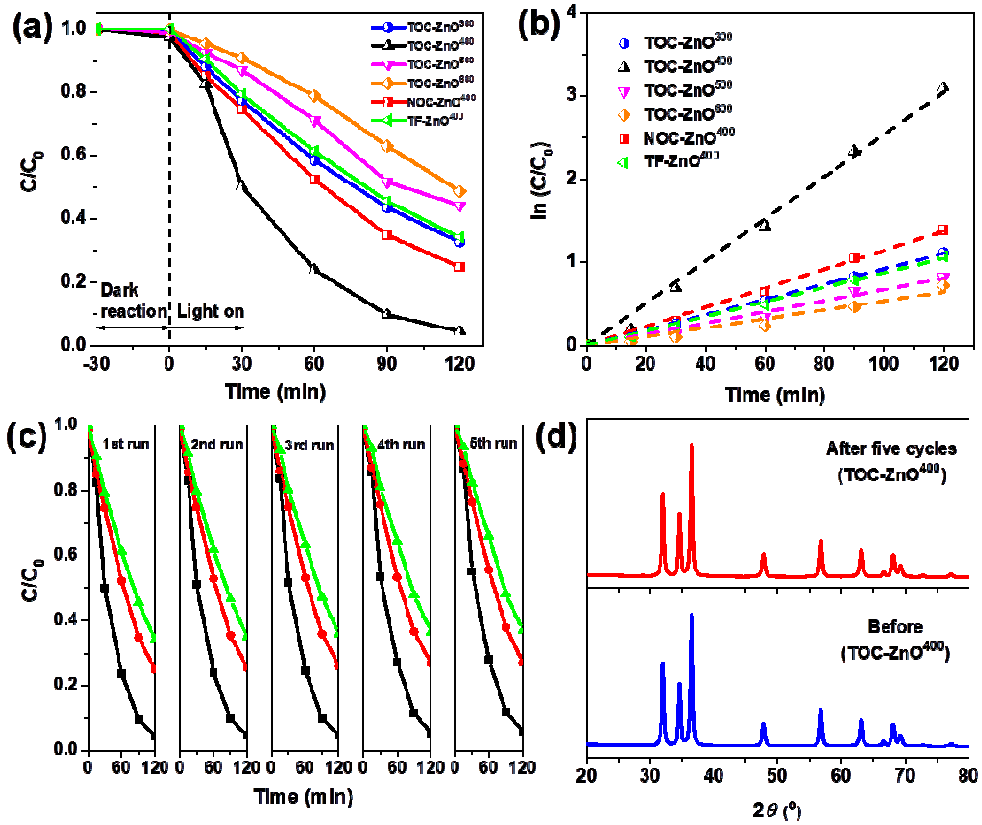

491

492 **Fig.7** Photocatalytic degradation curves of methyl orange by different ZnO^{x} samples (a) and (b);

493 reusability assessment of TF-ZnO^{400} (▲), NOC-ZnO^{400} (●) and TOC-ZnO^{400} (■) for methyl

494 orange photodegradation (c); XRD patterns of TOC-ZnO^{400} before and after photocatalytic

495 application for methyl orange (d).

496

497 **Table 1** Comparison of photocatalytic activity of TEMPO-oxidized cellulose-derived carbon

498 coated/doped ZnO with other recently reported ZnO photocatalysts

No.	ZnO samples	Cata. conc. (g L^{-1})	Degra. conc. (mg L^{-1})	Cata./ degra. (g/g)	UV-ir. (min)	Degra. (%)	Ref.
1	ZnO	0.5	10 (MO)	50	180	96.5	(Li, Lu & Luo, 2017)
2	ZnO	1.5	20 (MO)	75	100	81	(Gawade, Gavade, Shinde, Babar, Kadam & Garadkar, 2017)
3	ZnO	2	10 (MO)	200	210	92	(Kumar, Kumar & Umar,

							2013)
4	Cu-ZnO	0.5	10 (MO)	50	90	99.7	(Kadam, Kim, Shin, Garadkar & Park, 2017)
5	Al-ZnO	4	10 (MO)	400	120	95	(Lee, Kim, Park, Hong & Lee, 2015)
6	C-ZnO	0.4	4.8 (MB)	83.3	60	83	(Lee, Lim, Kang & Suh, 2015)
7	C-ZnO	2.5	5 (MB)	500	120	98	(Zhao, Zuo, Guo & Pan, 2017)
8	TOC-ZnO^{400}	0.25	5 (MO)	50	120	95.4	This work

499

500 Photocatalytic reusability of TOC-ZnO^{400}, NOC-ZnO^{400} and TF-ZnO^{400} were
501 investigated by reusing the catalysis in consecutive MO degradation reactions under
502 UV-irradiation. Before reuse, the catalysts were only washed with deionized water
503 and vacuum dried at 40°C. Figure 7-c displays that TOC-ZnO^{400}, NOC-ZnO^{400} and
504 TF-ZnO^{400} exhibit total photocatalytic durability after five cycles. Characterization by
505 XRD demonstrated the absence of structural change for TOC-ZnO^{400} before and after
506 photocatalytic performance (Figure 7-d).

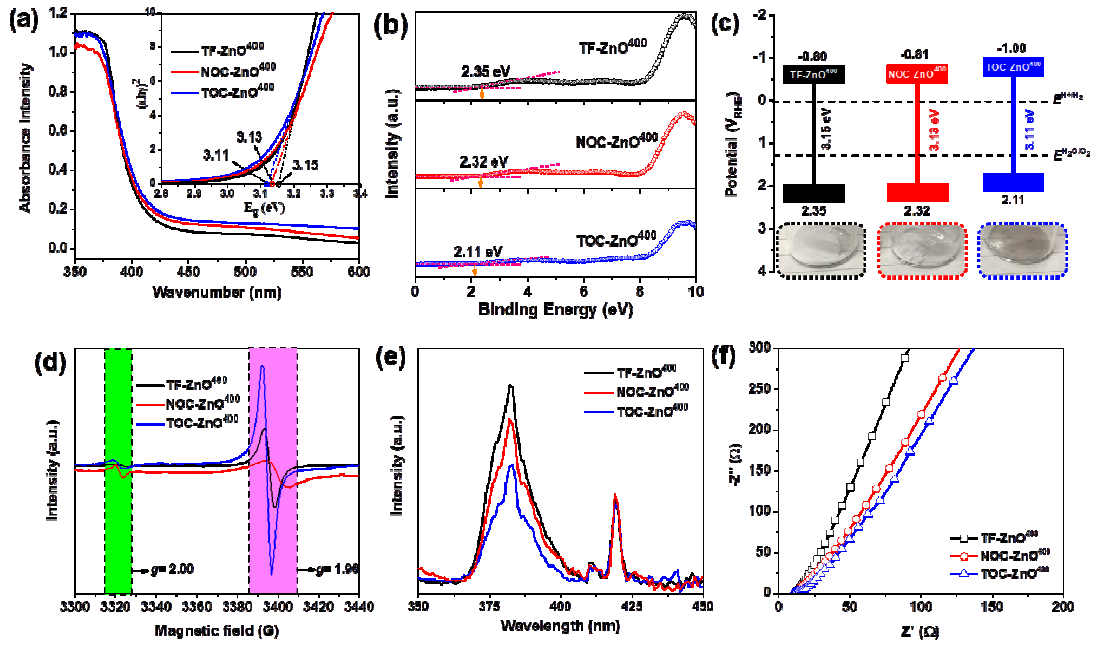

507

508 **Fig.8** Characterization of TF-ZnO^{400}, NOC-ZnO^{400} and TOC-ZnO^{400} by UV-vis DRS (a), XPS

509 spectra of all the samples for VB positions (b), VB and CB positions of all the samples (c), EPR
510 spectra (d), PL spectra (e) and EIS Nyquist plot (f).

511

512 *Photocatalytic mechanism.* To explore the mechanism of the photocatalytic activity of
513 carbon-coated ZnO obtained by calcination at 400°C, the band structures of
514 TF-ZnO^{400}, NOC-ZnO^{400} and TOC-ZnO^{400} have been probed. From Figure 8-a, the
515 UV-vis diffuse reflectance spectra of all the samples exhibited absorption in the UV
516 region (<400 nm). Compared with TF-ZnO^{400}, NOC-ZnO^{400} and TOC-ZnO^{400} have a
517 slightly red shifted absorption and possibly possess absorbance in the visible light
518 region, which is ascribed at present to the carbon doping of the ZnO nanocrystals(Jiao
519 et al., 2017; Zhang et al., 2015b). For the direct semiconductor ZnO, the band gap
520 energy was determined based on Tauc's equation(Shah et al., 2018):

521 $$\alpha h\gamma = A(h\gamma - E_g)^2$$

522 where α, A, γ, and E_g is the absorption coefficient, proportionality constant, light
523 frequency and band gap energy, respectively. From Figure 8-b, the band gap of
524 TF-ZnO^{400}, NOC-ZnO^{400} and TOC-ZnO^{400} are respectively 3.15 , 3.13 and 3.11 eV. In
525 order to measure the positions of conductive band (CB) and valence band (VB),
526 valence band potentials of all the samples were firstly detected by XPS
527 characterization. From Figure 8-b, the VB values of TF-ZnO^{400}, NOC-ZnO^{400} and
528 TOC-ZnO^{400} were 2.35 eV, 2.32 eV and 2.11 eV, respectively, which was obtained
529 from tangent lines with XPS spectra. Thus, according to the formula (E_g=*VB-CB*), CB
530 values of TF-ZnO^{400}, NOC-ZnO^{400} and TOC-ZnO^{400} were -0.80 eV, -0.81 eV and

-0.10 eV, respectively. CB and VB positions of all the samples are displayed in Figure 8-c; ZnO templated by cellulose, especially by TOC template, had shifted to the lower potentials with a narrower band.

EPR spectra were recorded in order to evaluate different defects (such as vacancies and interstitials) in ZnO through detecting the unpaired electron spins(Lv, Yao, Ma, Pan, Zong & Zhu, 2013). Oxygen vacancy is one of the important surface defects which can be caused by atom(C)-doping or appropriate thermal treatment(Polarz et al., 2006; Schneider et al., 2009) and Zinc interstitials (called Zn_i) is the other defect due to the incomplete annealing of the precursor(Zeng, Duan, Li, Yang, Xu & Cai, 2010). Both defects are important features of the material since it is known that such surface defects modify and possibly favor the adsorption and photocatalytic activities of catalysts. EPR spectra in Figure 8-d reveal different signals of the TF-ZnO^{400}, NOC-ZnO^{400} and TOC-ZnO^{400} ascribed to two kinds of defects in ZnO nanocrystals, namely zinc interstitials (Zn_i, g=1.96)(McCluskey & Jokela, 2009; Selim, Weber, Solodovnikov & Lynn, 2007) and oxygen vacancies (V_o, g=2.00)(Polarz et al., 2006). As shown in Figure 8-d, on the one hand, TOC-ZnO^{400} and NOC-ZnO^{400} are assumed to have higher intensities of oxygen vacancy than TF-ZnO^{400}, because of carbon associated with the ZnO nanocrystals, which is also in accordance with the XPS spectra. Abundant oxygen vacancies in the ZnO could further reduce the band gap in order to enhance the photocatalytic activity(Liu et al., 2014). On the other hand, the content of zinc interstitials of TOC-ZnO^{400} is significantly higher than TF-ZnO^{400} and NOC-ZnO^{400}, which might be ascribed to the

553 new bond formation of O-Zn-C as shown in Table S5. Besides, it is assumed that the
554 abundant oxygen defects and zinc interstitials also built enough vacancies and
555 exposed more active sites in order to enhance the photocatalytic activities(Kayaci,
556 Vempati, Donmez, Biyikli & Uyar, 2014; Wang et al., 2012).

557 In the photocatalytic processes, the majority of light absorption and subsequent
558 photo-excitation are usually generated on the surface of the photocatalyst, then
559 leading to the transfer and/or recombination of photo-induced electrons and holes.
560 Photoluminescence (PL) can be used to evaluate the separation or recombination rates
561 of photo-generated electron-hole carriers. A weak PL intensity reflects a low
562 recombination of photo-generated electron-hole carriers. From Figure 8-e, TF-ZnO^{400}
563 exhibited the strongest intensity and the PL intensity decreased in the order TF-ZnO^{400},
564 NOC-ZnO^{400} and TOC-ZnO^{400}. Although this difference can result from different
565 phenomenon, it is clear here that the increasing carbon and defect contents in the
566 samples are concomitant with a decrease of the PL intensity(Ansari, Ansari, Foaud &
567 Cho, 2017; Chen, Pang, An, Dittrich, Fan & Li, 2019). Although this C-content and
568 zinc/oxygen defects seem to reduce the recombination rates and enhance the
569 photocatalytic performance, the precise physical mechanism is not clear at present. In
570 order to get more evidences of such hypothesis, we compare the differences of
571 electron conductivity of the three samples in order to explain the transfer behavior of
572 photo-induced electrons. Electrochemical impedance spectroscopy (EIS) of ZnO
573 samples (Figure 8-f) was measured to go deeper in understanding the behavior of the
574 material and, eventually explain the difference inphotocatalytic activities. The slope of

575 EIS curve of TOC-ZnO^{400} is lower than NOC-ZnO^{400} and TF-ZnO^{400}, which indicated
576 that the former had higher electron transfer efficiency that can be ascribed to the
577 C-layer coating on the surface of the ZnO, significantly increasing electron transfer.
578 Thanks to fast transportation of photo-generated electrons, TOC-ZnO^{400} shows the
579 lowest PL intensity resulting from recombination of photo-generated electron-hole
580 carriers discussed above. Besides, it is known that carbon layer could adsorb more
581 ultraviolet and visible light yielding more photo-generated carriers (such as holes and
582 electrons). On the other hand, the doping of carbon in the ZnO lattice leads to the
583 formation of new mid-gap energy states above the valence band of O_{2p} orbitals of
584 ZnO mainly because of the existence of oxygen vacancies and causing to the
585 reduction of VB value(Alshammari et al., 2015; Liu et al., 2014). Above all, due to the
586 co-function of carbon coating and doping, the band gap of ZnO decreases and light
587 absorptions has a red-shift, which is favorable to the generated electrons easily
588 migrating to the conduction band. The photocatalytic reaction mechanism was shown
589 in Figure 9.

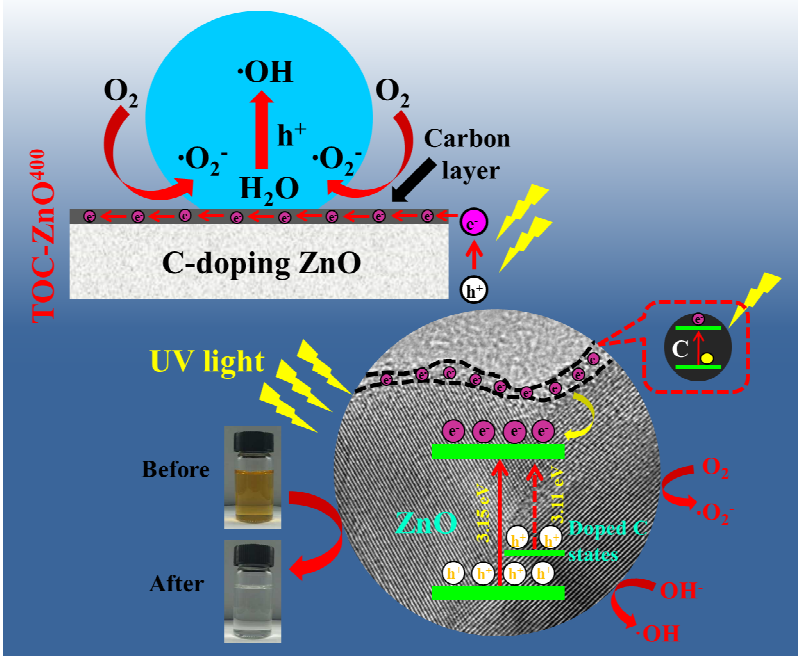

590

591 **Fig.9** Schematic illustration of the possible photocatalytic reaction mechanism of C-coated ZnO

592 obtained from TEMPO-oxidized cellulose.

593

594 **Conclusions**

595 This study introduces new elements on the great versatility of the use of cellulose as a

596 sacrificial biotemplate for the preparation of metal oxide/C functional nanocomposites

597 by hydrothermal process. It confirms that carboxyl-content control the morphology,

598 microstructures and particles size of the metal oxide, ZnO in the present case. We also

599 show that pyrolysis is not necessary to achieve the presence of nanocarbon associated

600 with ZnO, this can also be obtained by a careful control of the calcination of cellulose.

601 Concerning the photocatalytic activity of these materials, it is demonstrated that a thin

602 carbon layer onto ZnO increases the charge transfer and hydrophobicity of ZnO, a

603 narrowing of ZnO band gap and an increase of the zinc (V_{Zn}) and oxygen (V_o)

604 vacancies effectively suppressing of the charge recombination.

Acknowledgments

This work was supported by the National Key Research and Development Program of China (2017YFD601005), Natural Science Foundation of China (31700519, 21774021), Natural Science Foundation of Fujian (2018J01591), Science Fund of Fujian Provincial University (JK2017013), Distinguished Young Talents of Fujian Agriculture and Forestry University (XJQ201806), Award Program for Minjiang Scholar Professorship, Key Laboratory of State Forestry and Grassland Ministry (2019KFJJ16).

References

Abouzeid, R. E., Khiari, R., Beneventi, D., & Dufresne, A. (2018). Biomimetic mineralization of three-dimensional printed alginate/TEMPO-Oxidized cellulose nanofibril scaffolds for bone tissue engineering. *Biomacromolecules, 19*(11), 4442-4452.

Ali, A., Ambreen, S., Maqbool, Q., Naz, S., Shams, M. F., Ahmad, M., Phull, A. R., & Zia, M. (2016). Zinc impregnated cellulose nanocomposites: synthesis, characterization and applications. *Journal of Physics and Chemistry of Solids, 98*, 174-182.

Alshammari, A. S., Chi, L. N., Chen, X. P., Bagabas, A., Kramer, D., Alromaeh, A., & Jiang, Z. (2015). Visible-light photocatalysis on C-doped ZnO derived from polymer-assisted pyrolysis. *RSC Advances, 5*(35), 27690-27698.

Ansari, S. A., Ansari, S. G., Foaud, H., & Cho, M. H. (2017). Facile and sustainable synthesis of carbon-doped ZnO nanostructures towards the superior visible light photocatalytic performance. *New Journal of Chemistry, 41*(17), 9314-9320.

Beltran, J. J., Barrero, C. A., & Punnoose, A. (2019). Relationship between

ferromagnetism and formation of complex carbon bonds in carbon doped ZnO powders. *Physical Chemistry Chemical Physics, 21*(17), 8808-8819.

Boury, B., & Plumejeau, S. (2015). Metal oxides and polysaccharides: an efficient hybrid association for materials chemistry. *Green Chemistry, 17*(1), 72-88.

Cao, X., Ding, B., Yu, J., & Al-Deyab, S. S. (2012). Cellulose nanowhiskers extracted from TEMPO-oxidized jute fibers. *Carbohydrate Polymers, 90*(2), 1075-1080.

Chen, R., Pang, S., An, H., Dittrich, T., Fan, F., & Li, C. (2019). Giant defect-induced effects on nanoscale charge separation in semiconductor photocatalysts. *Nano Letters, 19*(1), 426-432.

Cheng, J., Ma, J., Ma, Y., Zhou, C., Qiang, Y., Zhou, X., Yang, J., Shi, H., & Xie, Y. (2018). Highly efficient ZnO-based dye-sensitized solar cells with low-cost Co-Ni/carbon aerogel composites as counter electrodes. *New Journal of Chemistry, 42*(19), 16329-16334.

Cheng, Q., Ji, L., Wu, K., & Zhang, W. (2016). Morphology-dependent electrochemical enhancements of porous carbon as sensitive determination platform for ascorbic acid, dopamine and uric acid. *Scientific Reports, 6*.

Cullity, B. D. (1978). Elements of X-ray diffraction. *Addison-Wesley Publishing Company, Inc.,* 2: 248.

Dong, S., Feng, J., Fan, M., Pi, Y., Hu, L., Han, X., Liu, M., Sun, J., & Sun, J. (2015). Recent developments in heterogeneous photocatalytic water treatment using visible light-responsive photocatalysts: a review. *RSC Advances, 5*(19), 14610-14630.

Foresti, M. L., Vazquez, A., & Boury, B. (2017). Applications of bacterial cellulose as precursor of carbon and composites with metal oxide, metal sulfide and metal nanoparticles: A review of recent advances. *Carbohydrate Polymers, 157*, 447-467.

Gawade, V. V., Gavade, N. L., Shinde, H. M., Babar, S. B., Kadam, A. N., & Garadkar, K. M. (2017). Green synthesis of ZnO nanoparticles by using Calotropis procera leaves for the photodegradation of methyl orange. *Journal of Materials Science-Materials in Electronics, 28*(18), 14033-14039.

Han, C., Yang, M.-Q., Weng, B., & Xu, Y.-J. (2014). Improving the photocatalytic activity and anti-photocorrosion of semiconductor ZnO by coupling with versatile

carbon. *Physical Chemistry Chemical Physics, 16*(32), 16891-16903.

Hewlett, R. M., & McLachlan, M. A. (2016). Surface structure modification of ZnO and the impact on electronic properties. *Advanced Materials, 28*(20), 3893-3921.

Hong, S. K., Lee, J. H., & Ko, W. B. (2011). Synthesis of 60 fullerene-ZnO nanocomposite under electric furnace and pPhotocatalytic degradation of organic dyes. *Journal of Nanoscience and Nanotechnology, 11*(7), 6049-6056.

Isogai, A., Saito, T., & Fukuzumi, H. (2011). TEMPO-oxidized cellulose nanofibers. *Nanoscale, 3*(1), 71-85.

Jiang, F., & Hsieh, Y. L. (2013). Chemically and mechanically isolated nanocellulose and their self-assembled structures. *Carbohydrate Polymers, 95*(1), 32-40.

Jiao, J., Wei, Y., Zhao, Y., Zhao, Z., Duan, A., Liu, J., Pang, Y., Li, J., Jiang, G., & Wang, Y. (2017). AuPd/3DOM-TiO_2 catalysts for photocatalytic reduction of CO_2: high efficient separation of photogenerated charge carriers. *Applied Catalysis B: Environmental, 209*, 228-239.

Kadam, A. N., Kim, T. G., Shin, D. S., Garadkar, K. M., & Park, J. (2017). Morphological evolution of Cu doped ZnO for enhancement of photocatalytic activity. *Journal of Alloys & Compounds, 710*, 102-113.

Kayaci, F., Vempati, S., Donmez, I., Biyikli, N., & Uyar, T. (2014). Role of zinc interstitials and oxygen vacancies of ZnO in photocatalysis: a bottom-up approach to control defect density. *Nanoscale, 6*(17), 10224-10234.

Kotsis, K., & Staemmler, V. (2006). Ab initio calculations of the O1s XPS spectra of ZnO and Zn oxo compounds. *Physical Chemistry Chemical Physics, 8*(13), 1490-1498.

Kumar, R., Kumar, G., & Umar, A. (2013). ZnO nano-mushrooms for photocatalytic degradation of methyl orange. *Materials Letters, 97*, 100-103.

Lee, H. J., Kim, J. H., Park, S. S., Hong, S. S., & Lee, G. D. (2015). Degradation kinetics for photocatalytic reaction of methyl orange over Al-doped ZnO nanoparticles. *Journal of Industrial & Engineering Chemistry, 25*, 199-206.

Lee, J., Lim, H. S., Kang, Y. S., & Suh, K. D. (2015). Carbon-doped ZnO submicron spheres functionalized with carboxylate groups and effect of dispersion stability in the

691 colloidal system for high photocatalytic activity. *RSC Advances, 5*(126),
692 104556-104562.
693 Lee, K. M., Lai, C. W., Ngai, K. S., & Juan, J. C. (2016). Recent developments of zinc
694 oxide based photocatalyst in water treatment technology: A review. *Water Research,*
695 *88*, 428-448.
696 Lefatshe, K., Muiva, C. M., & Kebaabetswe, L. P. (2017). Extraction of nanocellulose
697 and in-situ casting of ZnO/cellulose nanocomposite with enhanced photocatalytic and
698 antibacterial activity. *Carbohydrate Polymers, 164*, 301-308.
699 Li, B., & Cao, H. (2011). ZnO@graphene composite with enhanced performance for
700 the removal of dye from water. *Journal of Materials Chemistry, 21*(10), 3346-3349.
701 Li, J. Y., Lan, L., JianPing, X., XiaoSong, Z., HaiYan, L., & JinYan, Z. Controlled
702 growth of ZnO nanorods by polymer template and their photoluminescence properties.
703 *Science in China, 52*(4), 888-892.
704 Li, P., Lu, B., & Luo, Z. (2017). Hydrothermal growth of wheatear-shaped ZnO
705 microstructures and their photocatalytic activity. *Bulletin of Materials Science, 40*(6),
706 1069-1074.
707 Liu, D., Lv, Y., Zhang, M., Liu, Y., Zhu, Y., Zong, R., & Zhu, Y. (2014). Defect-related
708 photoluminescence and photocatalytic properties of porous ZnO nanosheets. *Journal*
709 *of Materials Chemistry A, 2*(37), 15377-15388.
710 Liu, S., Yao, K., Wang, B., & Ma, M.-G. (2017). Microwave-assisted hydrothermal
711 synthesis of cellulose/ZnO composites and its thermal transformation to ZnO/carbon
712 composites. *Iranian Polymer Journal, 26*(9), 681-691.
713 Lv, Y., Yao, W., Ma, X., Pan, C., Zong, R., & Zhu, Y. (2013). The surface oxygen
714 vacancy induced visible activity and enhanced UV activity of a ZnO_{1-x} photocatalyst.
715 *Catalysis Science & Technology, 3*(12), 3136-3146.
716 McCluskey, M. D., & Jokela, S. J. (2009). Defects in ZnO. *Journal of Applied Physics,*
717 *106*(7), 071101.
718 Mishra, D. K., Mohapatra, J., Sharma, M. K., Chattarjee, R., Singh, S. K., Varma, S.,
719 Behera, S. N., Nayak, S. K., & Entel, P. (2013). Carbon doped ZnO: synthesis,
720 characterization and interpretation. *Journal of Magnetism and Magnetic Materials,*

721 *329*, 146-152.
722 O'Connell, D. W., Birkinshaw, C., & O'Dwyer, T. F. (2008). Heavy metal adsorbents
723 prepared from the modification of cellulose: A review. *Bioresource Technology,*
724 *99*(15), 6709-6724.
725 Olaru, N., Calin, G., & Olaru, L. (2014). Zinc oxide nanocrystals grown on cellulose
726 acetate butyrate nanofiber mats and their potential photocatalytic activity for dye
727 degradation. *Industrial & Engineering Chemistry Research, 53*(46), 17968-17975.
728 Olivera, S., Muralidhara, H. B., Venkatesh, K., Guna, V. K., Gopalakrishna, K., &
729 Kumar, Y. K. (2016). Potential applications of cellulose and chitosan
730 nanoparticles/composites in wastewater treatment: A review. *Carbohydrate Polymers,*
731 *153*, 600-618.
732 Pan, L., Muhammad, T., Ma, L., Huang, Z. F., Wang, S. B., Wang, L., Zou, J. J., &
733 Zhang, X. W. (2016). MOF-derived C-doped ZnO prepared via a two-step calcination
734 for efficient photocatalysis. *Applied Catalysis B-Environmental, 189*, 181-191.
735 Patrinoiu, G., Calderon-Moreno, J. M., Birjega, R., Culita, D. C., Somacescu, S.,
736 Musuc, A. M., Spataru, T., & Carp, O. (2016). Sustainable one-pot integration of ZnO
737 nanoparticles into carbon spheres: manipulation of the morphological, optical and
738 electrochemical properties. *Physical Chemistry Chemical Physics, 18*(44),
739 30794-30807.
740 Pierre, G., Punta, C., Delattre, C., Melone, L., Dubessay, P., Fiorati, A., Pastori, N.,
741 Galante, Y. M., & Michaud, P. (2017). TEMPO-mediated oxidation of polysaccharides:
742 An ongoing story. *Carbohydrate Polymers, 165*, 71-85.
743 Polarz, S., Strunk, J., Ischenko, V., van den Berg, M. W. E., Hinrichsen, O., Muhler,
744 M., & Driess, M. (2006). On the role of oxygen defects in the catalytic performance
745 of zinc oxide. *Angewandte Chemie International Edition, 45*(18), 2965-2969.
746 Qu, Y., & Duan, X. (2013). Progress, challenge and perspective of heterogeneous
747 photocatalysts. *Chemical Society Reviews, 42*(7), 2568-2580.
748 Safwat, E., Hassan, M. L., Saniour, S., Zaki, D. Y., Eldeftar, M., Saba, D., & Zazou,
749 M. (2018). Injectable TEMPO-oxidized nanofibrillated cellulose/biphasic calcium
750 phosphate hydrogel for bone regeneration. *Journal of Biomaterials Applications,*

751 *32*(10), 1371-1381.
752 Samadi, M., Shivaee, H. A., Zanetti, M., Pourjavadi, A., & Moshfegh, A. (2012).
753 Visible light photocatalytic activity of novel MWCNT-doped ZnO electrospun
754 nanofibers. *Journal of Molecular Catalysis a-Chemical, 359*, 42-48.
755 Schneider, J. J., Hoffmann, R. C., Engstler, J., Dilfer, S., Klyszcz, A., Erdem, E., Jakes,
756 P., & Eichel, R. A. (2009). Zinc oxide derived from single source precursor chemistry
757 under chimie douce conditions: formation pathway, defect chemistry and possible
758 applications in thin film printing. *Journal of Materials Chemistry, 19*(10), 1449-1457.
759 Sehaqui, H., Zhou, Q., Ikkala, O., & Berglund, L. A. (2011). Strong and tough
760 cellulose nanopaper with high specific surface area and porosity. *Biomacromolecules,*
761 *12*(10), 3638-3644.
762 Selim, F. A., Weber, M. H., Solodovnikov, D., & Lynn, K. G. (2007). Nature of native
763 defects in ZnO. *Physical Review Letters, 99*(8), 085502.
764 Shah, N. S., Khan, J. A., Sayed, M., Khan, Z. U., Rizwan, A. D., Muhammad, N.,
765 Boczkaj, G., Murtaza, B., Imran, M., Khan, H. M., & Zaman, G. (2018). Solar light
766 driven degradation of norfloxacin using as-synthesized Bi^{3+} and Fe^{2+} co-doped ZnO
767 with the addition of HSO_5^- : Toxicities and degradation pathways investigation.
768 *Chemical Engineering Journal, 351*, 841-855.
769 Spathis, P. P., I. (1995). The corrosion and photocorrosion of zinc and zinc oxide
770 coatings. *Corrosion Science, 37*(5), 673-680.
771 Tran, D. T. (2016). Synthesis of porous ZnO based materials using an agarose gel
772 template for H_2S desulfurization. *RSC Advances, 6*(2), 1339-1345.
773 Vaiano, V., Matarangolo, M., Murcia, J. J., Rojas, H., Navio, J. A., & Hidalgo, M. C.
774 (2018). Enhanced photocatalytic removal of phenol from aqueous solutions using
775 ZnO modified with Ag. *Applied Catalysis B-Environmental, 225*, 197-206.
776 Wang, J., Wang, Z., Huang, B., Ma, Y., Liu, Y., Qin, X., Zhang, X., & Dai, Y. (2012).
777 Oxygen vacancy induced band-Gap narrowing and enhanced visible light
778 photocatalytic activity of ZnO. *ACS Applied Materials & Interfaces, 4*(8), 4024-4030.
779 Wu, X., Lu, C., Zhang, W., Yuan, G., Xiong, R., & Zhang, X. (2013). A novel
780 reagentless approach for synthesizing cellulose nanocrystal-supported palladium

781 nanoparticles with enhanced catalytic performance. *Journal of Materials Chemistry A,*
782 *1*(30), 8645-8652.
783 Xiao, H., Zhang, W., Wei, Y., & Chen, L. (2018). Carbon/ZnO nanorods composites
784 templated by TEMPO-oxidized cellulose and photocatalytic activity for dye
785 degradation. *Cellulose, 25*(3), 1809-1819.
786 Xiong, R., Lu, C., Wang, Y., Zhou, Z., & Zhang, X. (2013). Nanofibrillated cellulose
787 as the support and reductant for the facile synthesis of Fe_3O_4/Ag nanocomposites with
788 catalytic and antibacterial activity. *Journal of Materials Chemistry A, 1*(47),
789 14910-14918.
790 Yang, M.-Q., Weng, B., & Xu, Y.-J. (2013). Improving the visible light photoactivity
791 of In_2S_3-graphene nanocomposite via a simple surface charge modification approach.
792 *Langmuir, 29*(33), 10549-10558.
793 Yang, M.-Q., Weng, B., & Xu, Y.-J. (2014). Synthesis of In_2S_3-CNT nanocomposites
794 for selective reduction under visible light. *Journal of Materials Chemistry A, 2*(6),
795 1710-1720.
796 Yang, M.-Q., & Xu, Y.-J. (2013). Basic principles for observing the photosensitizer
797 role of graphene in the graphene-semiconductor composite photocatalyst from a case
798 study on graphene-ZnO. *Journal of Physical Chemistry C, 117*(42), 21724-21734.
799 Ye, S., Zhang, D., Liu, H., & Zhou, J. (2011). ZnO nanocrystallites/cellulose hybrid
800 nanofibers fabricated by electrospinning and solvothermal techniques and their
801 photocatalytic activity. *Journal of Applied Polymer Science, 121*(3), 1757-1764.
802 Yu, H.-Y., Chen, G.-Y., Wang, Y.-B., & Yao, J.-M. (2015). A facile one-pot route for
803 preparing cellulose nanocrystal/zinc oxide nanohybrids with high antibacterial and
804 photocatalytic activity. *Cellulose, 22*(1), 261-273.
805 Yu, W., Zhang, J., & Peng, T. (2016). New insight into the enhanced photocatalytic
806 activity of N-, C- and S-doped ZnO photocatalysts. *Applied Catalysis*
807 *B-Environmental, 181*, 220-227.
808 Yuan, Y., Fu, A., Wang, Y., Guo, P., Wu, G., Li, H., & Zhao, X. S. (2017). Spray
809 drying assisted assembly of ZnO nanocrystals using cellulose as sacrificial template
810 and studies on their photoluminescent and photocatalytic properties. *Colloids and*

Surfaces A-Physicochemical and Engineering Aspects, 522, 173-182.

Zeng, H., Duan, G., Li, Y., Yang, S., Xu, X., & Cai, W. (2010). Blue luminescence of ZnO nanoparticles based on non-equilibrium processes: defect origins and emission controls. *Advanced Functional Materials, 20*(4), 561-572.

Zhang, X., Qin, J., Hao, R., Wang, L., Shen, X., Yu, R., Limpanart, S., Ma, M., & Liu, R. (2015a). Carbon-doped ZnO nanostructures: facile synthesis and visible light photocatalytic applications. *The Journal of Physical Chemistry C, 119*(35), 20544-20554.

Zhang, X. Y., Qin, J. Q., Hao, R. R., Wang, L. M., Shen, X., Yu, R. C., Limpanart, S., Ma, M. Z., & Liu, R. P. (2015b). Carbon-doped ZnO nanostructures: facile Synthesis and visible light photocatalytic applications. *Journal of Physical Chemistry C, 119*(35), 20544-20554.

Zhang, Y., Zhang, N., Tang, Z.-R., & Xu, Y.-J. (2012). Graphene transforms wide band gap ZnS to a visible light photocatalyst. the new role of graphene as a macromolecular photosensitizer. *ACS Nano, 6*(11), 9777-9789.

Zhao, S.-W., Zuo, H.-F., Guo, Y.-R., & Pan, Q.-J. (2017). Carbon-doped ZnO aided by carboxymethyl cellulose: fabrication, photoluminescence and photocatalytic applications. *Journal of Alloys and Compounds, 695*, 1029-1037.

Zhou, P., Yu, J., & Jaroniec, M. (2014). All-solid-state Z-Scheme photocatalytic systems. *Advanced Materials, 26*(29), 4920-4935.